Journal of Solid State Chemistry **162,** 300–314 (2001)
doi:10.1006/jssc.2001.9319, available online at http://www.idealibrary.com on IDEAL®

Investigations of Nonstoichiometric Tungsten Oxide Nanoparticles

G. L. Frey,*[,1] A. Rothschild,*[,2] J. Sloan,†[,‡] R. Rosentsveig,* R. Popovitz-Biro,* and R. Tenne*[,3]

*Department of Materials and Interfaces, Weizmann Institute of Science, Rehovot 76100, Israel; †Inorganic Chemistry Laboratory, University of Oxford, South Parks Road, Oxford OX1 3QR, United Kingdom; and ‡Department of Materials, University of Oxford, Parks Road, Oxford OX1 3PH, United Kingdom

Received April 3, 2001; in revised form June 26, 2001; accepted July 16, 2001

IN HONOR OF PROFESSOR PAUL HAGENMULLER ON THE OCCASION OF HIS 80TH BIRTHDAY

Recently, pure phases of hollow multi-walled WS_2 nanotubes were prepared from a surface reaction with reduced tungsten oxide nanowhiskers. During the process, which starts with WO_{3-x} nanoparticles and finishes with WS_2 nanotubes, particular care has been devoted to the evolution of the tungsten oxide cores once the first encapsulating WS_2 layer has been formed. The reduced tungsten oxide phases were previously studied by a combination of techniques, including high-resolution transmission electron microscopy and X-ray diffraction. In the present study, Raman spectroscopy combined with the previous two techniques is used to give further detail concerning the structure of the reduced oxide phases. This study sheds some further light on the reduction process of the tungsten suboxide phases and the growth mechanism of oxide nanowhiskers and subsequently WS_2 nanotubes from quasi-isotropic tungsten oxide nanoparticles.

I. INTRODUCTION

Compounds of tungsten oxide with various stoichiometries have been documented. They were studied in the past in relation to their importance as, e.g., catalysts and electrochromic panels. By analogy with the synthesis of WS_2 fullerene-like particles from WO_3 nanoparticles (1, 2), pure phases of WS_2 nanotubes were grown recently starting from needle-like WO_{3-x} particles as a precursor (3, 4). In this reaction, the W–O bonds in the WO_{3-x} oxide precursor are progressively converted into W–S bonds (in WS_2) and the "outside in" reaction leads, after a few hours, to the formation of hollow multi-walled WS_2 nanotubes. Figure 1 shows a scanning electron micrograph of an assembly of WS_2 nanotubes grown from the WO_{3-x} precursor needles, which are elongated along one axis. In this process, the tungsten suboxide cores, which are encapsulated inside the WS_2 nanotubes, undergo a certain evolution. The microstructures of most of these encapsulated suboxides could be, at some point, described in terms of $\{hkl\}_R$ crystallographic shear (CS) planes relative to a ReO_3-type structure. Furthermore, the type of reduced CS phases encountered in the tungsten suboxide cores appeared to be directly dependent on the morphology of the sulfidized particles. Quasi-spherical faceted oxide nanoparticles, which are converted into nested fullerene-like nanoparticles (onions), were found to consist of a mixture of complex CS structures. Some oxide encapsulates with $\{103\}_R$ CS planes were also found (5). Usually, the encapsulated nanoparticles consisted of more than one oxide nanograin with clear grain boundaries separating the reduced oxide phases (1, 5). On the other hand, some suboxide phases encapsulated inside WS_2-nanotubes were found to form ordered $\{001\}_R$ CS planes (3, 5). Careful examination of the encapsulates using high-resolution electron microscopy (HRTEM) revealed that, although the CS were ordered along the growth axis of the encapsulated oxide nanowhisker, the distances between the CS planes were not always constant (3b, 5). In other cases, the $\{001\}_R$ CS formed two or more separated domains within the nanowhisker with a clearly observable boundary separating the two phases. Miyano *et al.* (6) described the $\{001\}_R$ CS in WO_{3-x} whiskers in terms of a homologous W_nO_{3n-1} series. Figures 2a and 2b show a schematic representation of the [010] projection of the $\{001\}_R$ CS phases of W_4O_{11} and W_5O_{14}, respectively (5). The CS planes are represented through the planes of edge sharing WO_6 octahedra. The reduction of the oxide entails that n decreases in this series and thereby WO_{3-x} is gradually converted into WO_2. This process can be described microscopically by a rapprochement of the CS walls separating the ReO_3 domains. A theoretical study of these phases (7) showed that elastic strain affects an attractive interaction between the CS domain walls, while for $n < 4$ a repulsive interaction predominates. This explains the great stability of shear structures with low

[1] Present address: OE group, Cavendish Laboratory, University of Cambridge, Madingly Road, Cambridge, CB3 0HE, United Kingdom.

[2] Present address: IMEC, SPT Division, Kapeldreef 75, B-3001 Leuven, Belgium.

[3] To whom correspondence should be addressed.

0022-4596/01 $35.00

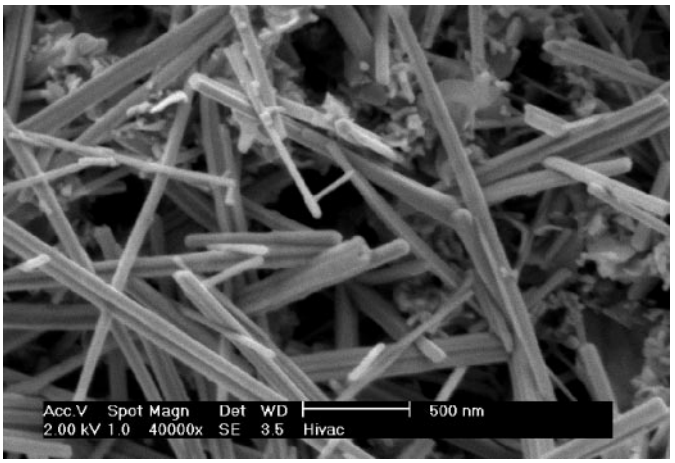

FIG. 1. Electron micrograph of an assembly of WS_2 nanotubes obtained by the sulfidization of oxide needle-like nanoparticles.

n number against complete reduction. The stability of these phases was of key importance in retaining a sufficiently open structure, which permitted slow diffusion of sulphur and oxygen at high temperatures and led to the formation of WS_2 nanotubes (3). Another stable phase in oxide whiskers is the γ-$W_{18}O_{49}$, which consists of an ordered 2-D lattice of edge-sharing WO_6 octahedra forming a network of pentagonal columns (PC) interspersed with hexagonal channels (HC) (8–10). This phase is represented schematically in Fig. 2c ([010] projection). No evidence for the existence of this phase in the encapsulated nanowhiskers was found in the previous study (5). Furthermore, a W_5O_{14} phase, which consists of PC and HC is known as well (11) and is schematically represented in Fig. 2d ([010] projection) [4]. These two latter phases are not only highly anisotropic, but they also possess a mechanical strength necessary for the holding together of the brittle oxide nanowhiskers during their growth and subsequent conversion into WS_2 nanotubes. Note that although the crystalline structures represented in Figs. 2b and 2d are very different, the O/W ratio for these two phases is the same (2.8).

In order to gain further understanding of the WS_2 nanotube growth mechanism, the evolution of the intermediate suboxides was studied during the reduction process. For this purpose, Raman scattering was used to follow the reduction process of the oxide nanowhiskers in addition to transmission electron microscopy (TEM), electron diffraction (ED), and high-resolution TEM (HRTEM). X-ray diffraction (XRD) was also performed in order to obtain more global information on the evolution of the crystalline structure of the nanoparticles during the reduction process. Whereas HRTEM and ED can be used to investigate the microstructure of a single nanowhisker, XRD provides global structural information concerning the sample, which contains many nanoparticles with various reduced phases. However, because of line broadening effects due to the latter, the interpretation of the XRD data is not unambiguous. Raman spectroscopy is situated somewhat in between the two extremes, since the optical beam can be focussed to domains of 1 micro-meter and, if the sample is well dispersed, a few nanowhiskers or even a single nanostructure can be probed, provided the intensity of the signal is sufficiently large.

Unfortunately, the cross-section (σ) for Raman scattering and the absorption coefficient (α) of the encapsulating WS_2 layers are much larger than those of the suboxide phases inside the nanoparticle core. For this reason it was not possible to detect the Raman signal originating from the encapsulated suboxides using the present setup. To bypass this problem, an alternative strategy was employed. Indeed, long oxide (WO_{3-x}) whiskers (several micro-meters in length) can be produced, starting from precursor needle-like WO_{3-x} particles (50 nm in length) by annealing the latter at 840°C under a gas mixture of H_2/N_2 (3, 4). It was often observed that reduced oxides with ordered superstructures, similar to those oxides formed within the WS_2 nanotubes, occur in the elongated nanowhiskers. Taking advantage of this similarity, the evolution of the tungsten suboxides under the reductive hydrogen atmosphere was investigated. There appears to exist a relationship between the degree of reduction of the WO_3 nanoparticles; their morphology, and their crystalline structure. Whereas the pure WO_3 nanoparticles are essentially isotropic, the shape of the reduced nanoparticles (WO_{3-x}) is generally elongated. This evolution is attributed to the evolution of the lattice structure (see below).

Furthermore, the crystalline structure of WO_3 is quite isotropic, but the lattice parameters of the various suboxide phases are highly anisotropic. Moreover, the crystal structure of WO_2 is again quite isotropic, which explains the tendency of this oxide phase to adopt a more symmetric morphology. Thus, the reduced tungsten-oxide phases go through a cascade of phase transformations during reduction, which affects their stoichiometry, and also their morphology. Three types of tungsten oxide nanoparticles were used as precursors in this study. The first type, commercially available, was made of WO_3 nanoparticles with a yellow tint. This phase served as a precursor for the synthesis of WS_2 nanotubes, using the fluidized bed reactor (see below). The oxide nanowhiskers were obtained by either interrupting the reaction after a few minutes, or by having a too little H_2S flow in the reactor. The other two types of tungsten

[4] To distinguish the two forms of W_5O_{14} oxides based on CS planes and HC columns, we use the notation CS-W_5O_{14} for the crystal shear (i.e., Miyano) form of this phase and HC-W_5O_{14} for the form containing hexagonal channels.

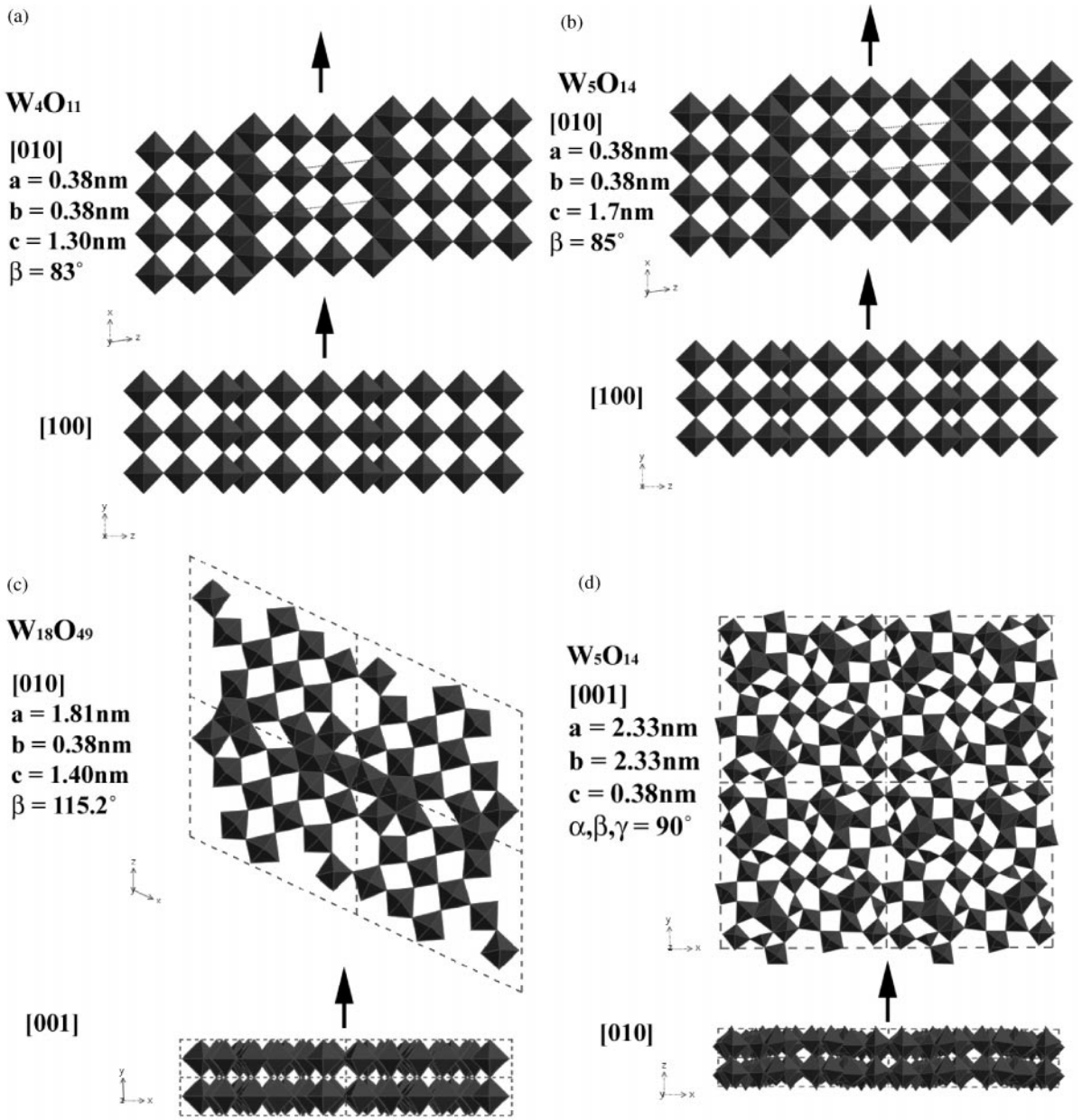

FIG. 2. Schematic representation of various reduced tungsten oxide phases with $\{001\}_R$ CS (the W_nO_{3n-1} family of phases): (a) CS-W_4O_{11} lamellar phase (6); (b) CS-W_5O_{14} lamellar phase (6); (c) cross section ([010] direction) of a γ-$W_{18}O_{49}$ phase containing a network of PC and HC; (d) cross section ([010] direction) of HC-W_5O_{14} with a network of PC and HC. The arrows show the growth direction of the nanowhisker.

suboxides precursors (types I and II) were prepared in-house by a documented procedure (3) (see below). Type I consists of quasi-spherical faceted particles, while type II is composed predominantly of needle-like particles. Both types of precursor were studied by a combination of TEM, HRTEM, and XRD. Analysis with Raman scattering, which has not been used for characterization of these types of materials so far, is being reported in this work.

II. EXPERIMENTAL SECTION

II.1. Preparation of the Samples

II.1.a. Synthesis of the WO_{3-x} particles (type I and type II precursors). A few tens of mg of tungsten suboxide particles (WO_{3-x}) were produced by heating a tungsten filament (model ME11 from the R. D. Mathis company) in the presence of water vapor inside a vacuum chamber (3). The

following procedure was used: a tungsten filament was preheated for a few minutes in an evacuated (10^{-4} Torr) bell-jar in order to remove the superficial oxidized layer. Water vapor was then allowed to diffuse into the vacuum chamber through an inlet, until the desired pressure was reached (additional argon was sometimes introduced into the chamber in order to increase the total vapor pressure). The filament was then heated to around $1600 \pm 20°C$, while the pressure in the chamber was maintained at a constant value of a few Torr during the evaporation process. After a few minutes of evaporation, a blue powder condensed on the bell-jar walls. Depending on the water vapor pressure and the total pressure in the chamber, the accrued powder consisted of either amorphous material, or faceted and isotropic nanoparticles (type I, 25 nm in diameter) or needle-like particles (type II, 50 nm in length and 15 nm in diameter) (3b). These nanoparticles could be converted quantitatively into WS_2 nanotubes.

II.1.b. Reduction of the WO_{3-x} precursors (types I and II). The progressive reduction of both types of WO_{3-x} particles (isotropic faceted, type I; needle-like, type II) was performed in a reactor heated to 840°C under the flow of a 1% H_2/99% N_2 gas mixture. The flow-rate was maintained constant during all the experiments (200 $cm^3\,min^{-1}$), while the reaction time was increased progressively from one batch to another. Starting with type I particles, five samples corresponding to a reduction period of 1, 5, 10, 20, and 60 min were prepared. The same procedure was repeated with the particles of type II (needle-like), and led to a series of five samples corresponding to a reduction time of 2, 5, 10, 15, and 60 min.

II.1.c. Synthesis of WO_{3-x} nanowhiskers using the fluidized bed reactor. More recently, a fluidized bed reactor for the synthesis of large amounts (20–30 g/day) of nested fullerene-like WS_2 nanoparticles from quasi-spherical WO_3 nanoparticles has been constructed (12). A slightly modified reactor of this kind was found to produce WO_{3-x} nanowhiskers and subsequently WS_2 nanotubes in large amounts in a single process using commercially available WO_3 nanoparticles (METEK Technologies). However, a pure phase of the nanotubes has not so far been obtained (13). The separation of nanotube bundles from the nanoparticles by a system of sieves has been shown to be achievable (13). In some cases, the sulfidization of the oxide nanoparticles was not complete and thus, oxide nanowhiskers were found at the end of the reaction.

II.2. X-Ray Powder Diffraction (XRD), Transmission Electron Microscopy (TEM), and High-Resolution Transmission Electron Microscopy (HRTEM)

XRD of the samples were measured in the transmission mode (0.3 mm glass capillaries) of a Rigaku Rotaflex RU-200B apparatus having a Cu$K\alpha$ anode. The samples were also analyzed by a TEM (Philips CM-120 (120 kV)) supplemented by a JEM-4000EX HRTEM operated at 400 kV. The electron diffraction (ED) patterns were obtained on the HRTEM instrument and these were calibrated using TlCl as a reference standard. The accuracy of the d_{hkl} spacings was estimated to be $\pm$ 0.005 nm.

II.3. Raman Scattering

Raman spectra were recorded by a Renishaw 1000 Raman microscope at ambient temperatures using a standard backscattering geometry. An excitation wavelength corresponding to the 623.8 Å line of a He/Ne laser, which was capable of supplying 1 mW of power was used. In order to prevent damage to the samples, an optical fiber was used to reduce the incident power to roughly 0.6 mW. In addition, a constant flow of Ar gas over the sample prevented oxidation of the particles. Several regions from each sample were probed to ensure reproducibility of the data. Scattering intensities were measured using a high-resolution CCD camera.

III. RESULTS AND DISCUSSION

III.1. Study of the Reduction Effect on the WO_{3-x} Particles by TEM/HRTEM and ED

With respect to the quasi-spherical precursors (i.e., type I nanoparticles), the reduction was accompanied by rapid densification of the samples, and the specimens generally became tinted and more opaque in the TEM as the reduction proceeded. Starting with the needle-like particles (i.e., type II particles) led also to the same observation. Indeed, as was evidenced by ED patterns, both sets of samples went through an overall reduction process from WO_{3-x} to W *via* a wide series of reduced tungsten oxide intermediates, such as WO_2 (Table 1a). A clear correlation could be observed between the morphology of the particles, as they appeared in the TEM, and their stoichiometry, which was determined by ED. Indeed, the further the reduction process has proceeded, the less WO_{3-x} whiskers were present and more faceted spheroidal WO_2 or W particles appeared in the products (Tables 1a and 1b). The global mechanism could therefore be summarized as follows. A first step, which goes through a wide variety of tungsten suboxides intermediates, and ends up with the formation of WO_2 particles. Then, a second step follows, which leads to the production of tungsten particles

$$WO_{3-x} + H_2 \rightarrow WO_2 + (1-x)\,H_2O + xH_2 \qquad [1]$$

$$WO_2 + 2H_2 \rightarrow W + 2H_2O \qquad [2]$$

TABLE 1a
Evolution of the Morphology of the WO_{3-x} Particles with the Reduction Time (ED Analysis)

Type I precursor (spherical-faceted particles)		Type II precursor (needle-like particles)	
Reduction time (min)	Stoichiometry (ED)	Reduction time (minutes)	Stoichiometry (ED)
2	W_nO_{3n-2} ($W_{20}O_{58}$)	1	W_nO_{3n-2} ($W_{20}O_{58}$)
5	$WO_2 + \pm W_{20}O_{58}$ + few W_nO_{3n-1}	5	$\pm W_{20}O_{58} + W_nO_{3n-1}$ ($n = 4, 5, 6$) + very few WO_2 + ($W_{18}O_{49}$)*
10	WO_2	10	$\pm W_{20}O_{58} + W_nO_{3n-1}$ ($n = 4, 5, 6$) + more WO_2
15	WO_2	20	$WO_2 + W$
60	$WO_2 + W$	60	W

Note. The gas mixture going through the reactor is 1%H_2/99% N_2 and its flow-rate 200 $cm^3\,min^{-1}$. Sh denotes short whiskers, L denotes long whiskers, "S–F" denotes spherical-faceted particles, * has been found by HRTEM.

The densities of the WO_{3-x} precursor (ca. 7.16 $g\,cm^3$) and the reduced tungsten metal (19.35 $g\,cm^3$) (14), are therefore consistent with the densification phenomenon, which occurs during the overall process. Both WO_2 (distorted rutile) and W (fcc) possess more or less an isotropic crystalline habit, while the reduced suboxide WO_{3-x} phases are highly anistropic in their crystalline structure. Not surprisingly therefore, the chemical transformation of the WO_{3-x} phases into WO_2 and subsequently into W is followed by a change from highly anisotropic to a more or less isotropic morphologies (see below).

It appears that, whatever the original WO_{3-x} precursor (i.e., types I or II), very long oxide whiskers (several micrometers in length) are formed at the early stages of the reduction process (i.e., within the first 5 min, or less). However, the proportion of these whiskers compared to spherical-faceted particles is clearly dependent on the type of precursor. While after 5 min reduction, type I particles consisted of spherical-faceted particles as the majority product, type II particles were predominantly long oxide whiskers (Table 1b). As the reduction proceeds, the batches were also distinguished by a time-lag between the appearance of the new reduced phases. In the case of type II precursor (Fig. 3a), the long nanowhiskers (N) that have been formed during the first instant of the reduction period (< 1 min) mostly preserved their shape after a 5 min reduction time. However, their cores were found to be reduced to WO_2 (see also Tables 1a and 1b). For the same reduction period (5 min) the type I precursor are quickly transformed from elongated WO_{3-x} nanoparticles into WO_2 spherical-faceted nanoparticles with fully reduced metallic cores (Fig. 3b). It is to be noted, that in the case of type I oxide nanoparticles, the presence of H_2S gas in the reaction atmosphere led to a rapid encasing of the oxide nanoparticles by a few WS_2 layers, and the quasi-spherical shape of the nanoparticles is therefore preserved (1). Also, typically {102} or {103} CS planes were found in the reduced oxide core of such nanoparticles (5). The rate of reduction of the oxide was also found to be slowed down considerably in the case of the WS_2 encapsulated WO_{3-x} nanoparticles. Whereas complete reduction into WO_2 and subsequently into W metal may take place within a few minutes, for the bare oxide type I nanoparticles, the WO_{3-x} core of the WS_2 enfolded nanoparticles is stable for a few hours under similar reducing conditions.

TABLE 1b
Evolution of the Morphology of the WO_{3-x} Particles with the Reduction Time (TEM Observations)

Type I precursor (spherical-faceted particles)		Type II precursor (needle-like particles)	
Reduction time (min)	Morphology (TEM)	Reduction time (min)	Morphology (TEM)
2	Sh + L	1	Sh
5	"S-F" $\gg$ L	5	L $\gg$ "S-F"
10	"S-F"	10	L $\gg$ "S-F"
15	"S-F"	20	"S-F"
60	"S-F"	60	"S-F"

Note. The gas mixture going through the reactor is 1%H_2/99% N_2 and its flow-rate 200 $cm^3\,min^{-1}$. Sh denotes short whiskers, L denotes long whiskers, "S-F" denotes spherical-faceted particles, * has been found by HRTEM.

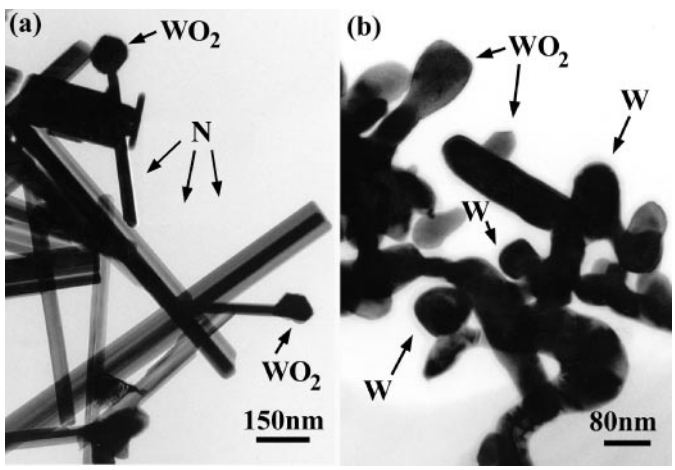

FIG. 3. TEM micrographs of the evolution of types II and I precursors after 5 min reduction. (a) Type II precursor: a long oxide nanowhisker, representative of the batch. While the shell of the nanowhisker consists of a WO_{3-x} phase, the core is further reduced to WO_2. (b) Type I precursor: mostly spherical-faceted particles of WO_2 and W core are observed.

Figures 4a–4d document a series of reduced intermediates observed in the oxide needles across the composition range WO_3–WO_2. Figure 4a shows a WO_3 oxide needle in the early stages of reduction. The microstructure conforms to that of well-ordered monoclinic WO_3 viewed along [100]. A small amount of disorder is indicated by the diffuse streaking along [001] in the Fourier transform (FFT) image (inset). Note that in this whisker, the growth axis is along the [010] direction. Figure 4b shows a typical nonstoichiometric WO_{3-x} needle observed within a more reduced preparation. The extent of disorder in this intermediate is clearly indicated in the inset ED pattern as parallel rows of diffuse streaked reflections indicating disorder orthogonal to the needle axis (bold arrow, inset). The disorder can possibly be attributed also to the formation of oxygen vacancy walls, which were postulated to precede the formation of the CS planes or, alternatively, the formation of random CS planes within the needles (15, 16). In Fig. 4c, a lattice image corresponding to an ordered intermediate is shown which, in this case, conforms to a [110] projection of $W_{18}O_{49}$ (γ-tungsten oxide). It is important to emphasize here, that this is only one of a number of possible ordered intermediates and others were observed. Figure 4d shows an [100] projection of an ordered fragment corresponding to the WO_2 phase.

The example in Figs. 5a–5c shows a twinned version of an identical projection of the $W_{18}O_{19}$ phase shown in Fig. 4c. A lower magnification micrograph in Fig. 5a shows a prominent twin boundary (arrowed) which is also visible in the corresponding ED pattern (Fig. 5b) as splitting of the reflections in the noncentral rows. The indicated pair of spots in Fig. 5b correspond to split ($1\bar{1}3$) reflections (cf. Fig. 4c, inset). Figure 5c shows an enlargement of the microstructure of the encapsulate, which is clearly identical to that in the micrograph in Fig. 4c. The observed oxide needle is encased within two layers of the encapsulating sulphide, which is an early stage in the growth of the WS_2 nanotube. An important new observation arising from this work is that, with respect to *IF*-WS_2 encapsulated tungsten oxides, the encapsulation process is apparently independent of the ordering behavior of the encapsulated oxide. Previously we noted the formation of ordered tungsten oxides within *IF*-WS_2 cages. The encapsulated oxide in Fig. 5 is clearly the same oxide as the ordered precursor in Fig. 4c. This is consistent with the observation, also made in the previous work, that disordered tungsten oxides are also observed within *IF*-WS_2 structures. This does not necessarily rule out the possibility of ordering during encapsulation, which invariably involves some heat treatment and reduction of the precursors. However the previously noted ordering phenomenon is an incidental rather than essential feature of the encapsulation process and the sulfidization reaction is a surface rather than a bulk phenomenon. A consequence of this observation is that it ought to be possible to tailor the type of

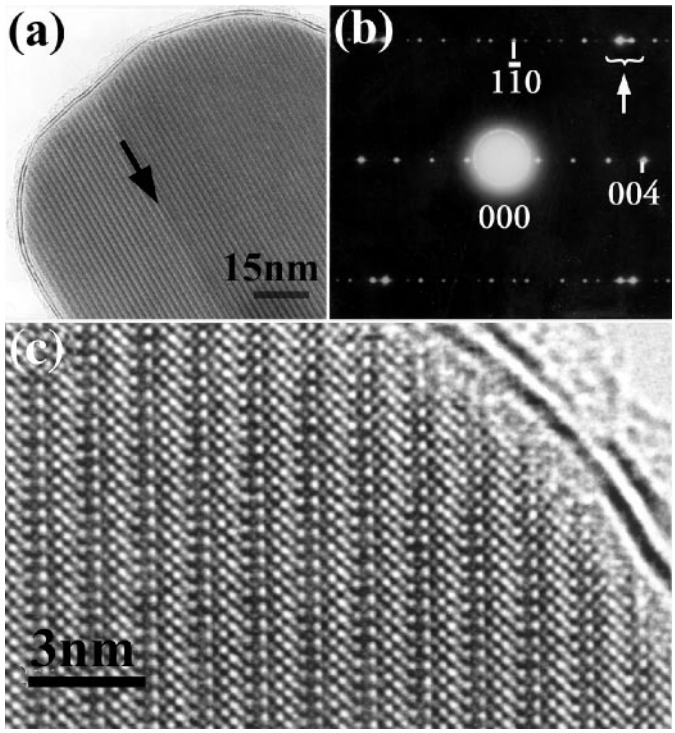

FIG. 5. TEM image of a twinned nanowhisker of the $W_{18}O_{19}$ phase, which is encapsulated by closed WS_2 layers.

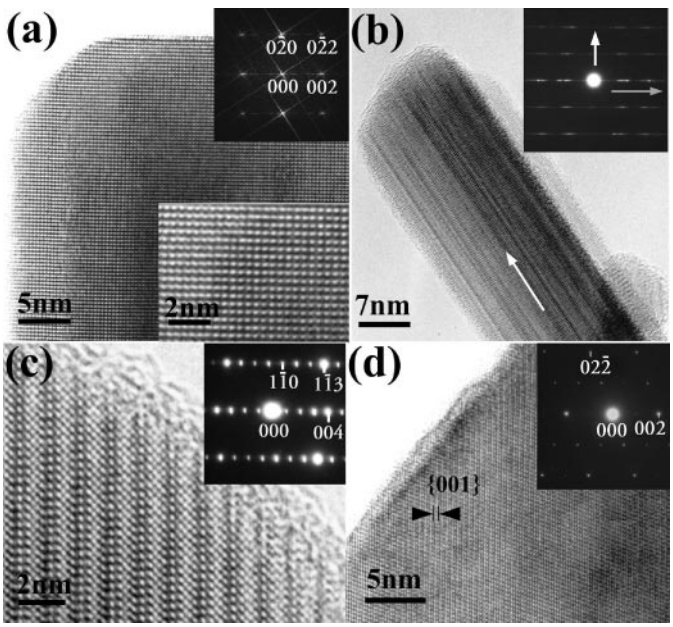

FIG. 4. TEM images of a series of reduced intermediates observed in the oxide needles across the composition range WO_3–WO_2. (a) WO_3 oxide needle in the early stages of reduction; (b) typical nonstoichiometric WO_{3-x} needle; (c) [110] projection of $W_{18}O_{49}$ (γ-tungsten oxide); (d) [100] projection of an ordered WO_2 crystallite.

tungsten oxide encapsulate produced within *IF*-WS_2 materials, although given the complexity of the WO_3–WO_2 system, this is a far from trivial exercise.

Concerning the type of defects encountered in the tungsten suboxides core, it was observed that many whiskers are indeed composed of well distinguishable "strips" in the [010] direction, which is evidence of the presence of $\{001\}_R$ crystallographic shear (CS) planes along the growth direction [010]. The CS defects are found to be randomly distributed inside the core of the whiskers and their density varied from one whisker to another. Consequently, the stoichiometry of the whiskers is extremely variable (WO_{3-x} with x variable), which leads to a wide mixture of non-stoichiometric phases in the early stages of the reduction. As the reduction time increases, more and more $\{001\}_R$ CS planes are created and start to approach each other, ending up with a fully ordered stoichiometric structure of the form: W_nO_{3n-1} (4, 5) or W_nO_{3n-2} (17, 18). Alternatively, stable PC motifs are formed along the nanowhiskers. Such ordered structures inside the whiskers have been routinely observed in the samples originated from type II precursor, already after 5 min annealing (Fig. 5). It is important to notice that no other type of defects were apparently created in the long tungsten oxide whiskers. This fact underscores the importance of the $\{001\}_R$ CS planes and the PC motifs in the formation of WS_2 nanotubes from needle-like tungsten oxide nanoparticles (1).

A second point to emphasize is that the rate of reduction of the spherical oxide nanoparticles is fast under these conditions, and consequently, in contrast to the case of *IF*-WS_2 nanoparticles with oxide core (5), no definitive answer regarding the type of defects could be obtained. The small fraction of spherical nanoparticles (type I), which are converted into nanowhiskers contain $\{001\}_R$ CS planes and superstructures with PC, exclusively. This fact tends to demonstrate that $\{001\}_R$ CS planes or an array of PC and HC are the only defects compatible with the growth and evolution of the nanowhisker morphology. This is not surprising in view of the large anisotropy, typical of such crystalline structures and consequently their high mechanical strength, which can support these long and slender nanostructures made of quite a brittle material.

By examining the samples with a HRTEM, the same general conclusions could be drawn. Unexpectedly however, another phase could be distinguished that was not observed by the preceding TEM studies (3, 5). Indeed, the γ-$W_{18}O_{49}$ phase (8), consisting of pentagonal columns (PC) and hexagonal channels (HC), was observed in the batches originated from type II precursors (see Table 1a). This point is particularly noteworthy and it will be further discussed in what follows.

Generally, the nanotubes produced by the fluidized bed reactor are longer (up to 300 μm) than the nanotubes reported earlier (3). Furthermore they grow open ended instead of the closed ended nanotubes reported previously (3). In these two respects they are more closely related to the WS_2 nanotubes reported in (4). This entails that in contrast to the previous report (3), here the oxide nanowhisker grows first and crystallize (probably in the upper part of the reactor), and are subsequently sulfidized (in the lower part of the reactor). The partially converted nanowhiskers are obtained by interrupting the reaction some 15 min after it has started. TEM images of the tungsten oxide nanowhiskers obtained by the fluidized bed reactor are shown in Figs. 6–8. Figure 6a shows a TEM image of a bunch of nanowhiskers, which were part of a material identified (by XRD) as belonging to the HC-W_5O_{14} phase. Figure 6b shows the TEM image of a tip of single nanowhisker and its ED in the inset. The long *d*-spacing of 11.6 Å was assigned as the (200) reflection of the HC-W_5O_{14} phase. Figure 7 shows an *IF*-WS_2 nanowhisker encapsulating a reduced oxide core. Figure 7a shows the image of the whole nanowhisker under a low magnification. In Fig. 7b, the magnified image of the nanowhisker tip is shown. The pencil-shaped tip is open at the end. Most remarkably, while the oxide nanowhisker is encapsulated by two layers of WS_2, the number of WS_2 layers increases at the whisker tip to six. The image also clearly reveals the lattice image of the oxide phase in the

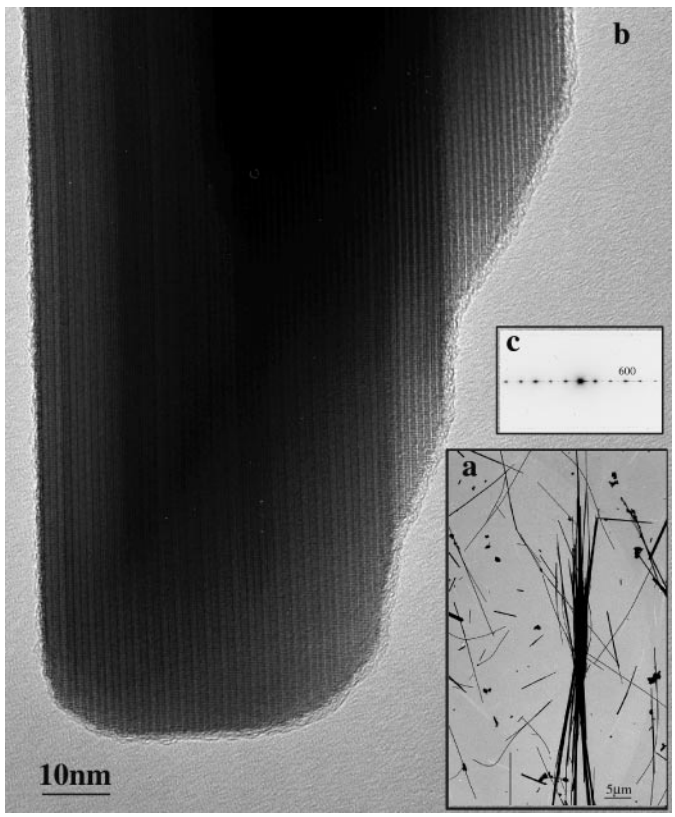

FIG. 6. TEM micrograph of an oxide nanowhisker produced by the fluidized bed reactor. The HC-W_5O_{14} was identified through ED.

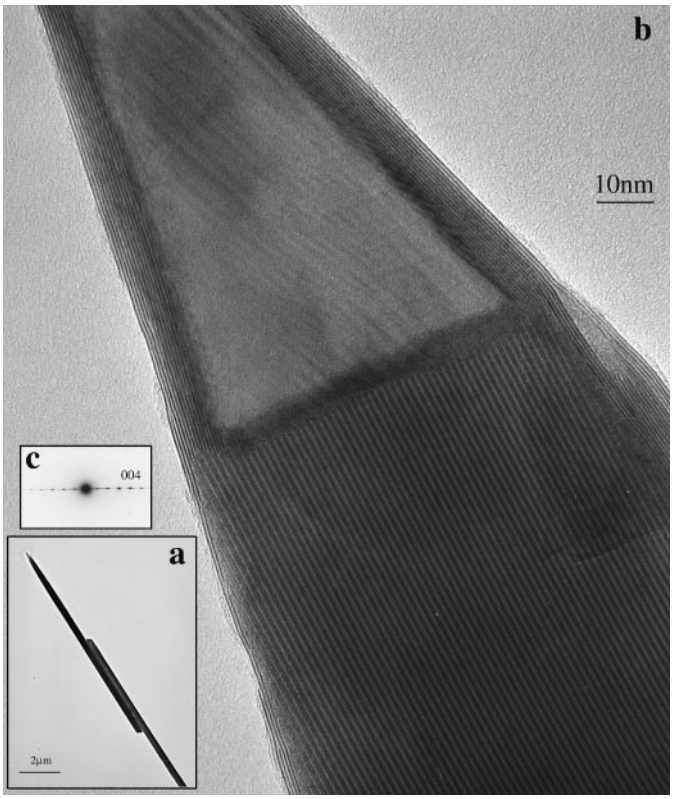

FIG. 7. A pencil-shaped oxide nanowhisker encapsulated by closed WS_2 layers. The oxide is assigned to the $W_{18}O_{49}$ phase. Note that the tip of the nanowhisker is open, i.e., the sulfide layer is not closed at this end. Note also that the number of encapsulating WS_2 layers is 2 in the bulk of the nanowhisker and increases to 6 at the tip.

core. The electron diffraction of the oxide core is shown in Fig. 7c. The long spacing of 12.7 Å could be assigned to the (001) reflection of the $W_{18}O_{49}$ phase. In other series of growth experiments however, the spacing of the diffraction dots of the oxide core (16.5 Å) coincided with that of the CS-W_5O_{14} phase, i.e., the one belonging to the $\{001\}_R$ CS series, which was discussed in detail in (5). Figure 8a shows a [010] view of a fragment of a broken $W_{18}O_{49}$ nanowhisker. This fragment appears to be a pure phase with no obvious defects. The enlargement in Fig. 8b shows that this fragment consists of an ordered array of pentagonal column (PC) units interspersed with domains of ReO_3-type WO_3 structure and hexagonal channels (HC). Figures 8c and 8d show an image simulation and structure model corresponding to the same projection of $W_{18}O_{49}$. The unit cell of this phase is indicated by the parallelogram in Figs. 8b–8d.

It is thus found that while the unencapsulated nanowhiskers can adopt a number of different oxide phases, the core of the *IF*-WS_2 nanowhiskers is predominantly made of the anisotropic $W_{18}O_{49}$ phase, which is typified by a network of PC and HC. Notably the present product contains also large amount of WS_2 nanoparticles with nested fullerene-like structure.

The reduction of WO_3 in the fluidized bed reactor is accompanied by a unique morphological change, from round or elongated small WO_3 particles to whiskers ranging from a few to about 50 μm in length. Two phases of WO_{3-x} whiskers have been identified by electron diffraction. HC-W_5O_{14} ($WO_{2.8}$) that packs in a tetragonal space group P-421m $a = b = 2.33$, $c = 0.38$ nm and $W_{18}O_{49}$ ($WO_{2.72}$) that belongs to a monoclinic space group $P2/m$ $a = 1.83$, $b = 0.38$ and $c = 1.4$ nm. These two phases have pentagonal columns and pseudo-hexagonal channels running along the whisker. The growth morphologies of these whiskers can be related to their crystallographic structures using the Bravais–Friedel–Donnay–Harker (BFDH) law as the rule of thumb (19). According to this law the growth rate of a crystal face is inversely proportional to the interplanar spacing of that face. Thus, in both WO_{3-x} phases observed, the growth direction of the whisker is the short 0.38 axis, while the larger and more developed faces are those with the largest interplanar spacing. This is in contrast to the precursor WO_3 that in all its polymorphs has three rather similar cell dimensions, with no preferred growth direction.

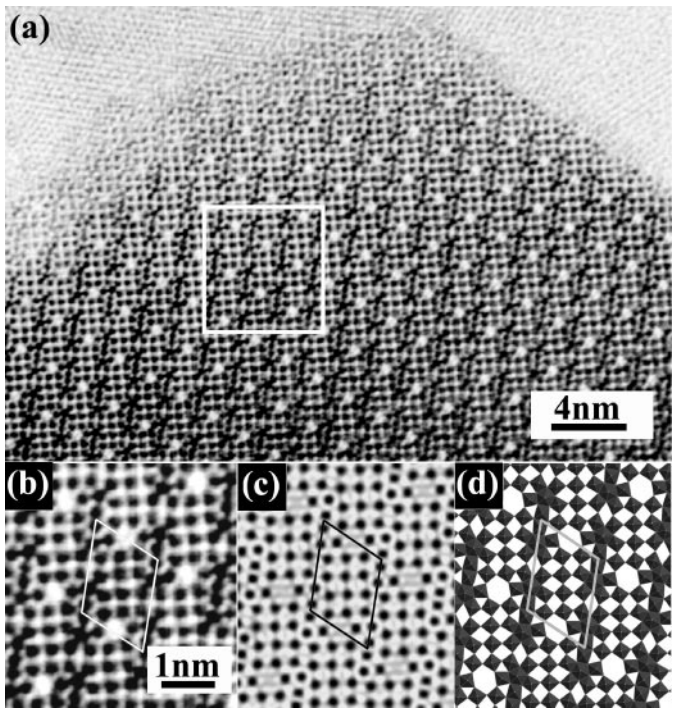

FIG. 8. (a) Low magnification HRTEM micrograph showing the regular microstructure of a $W_{18}O_{49}$ fragment; (b) Enlargement of boxed region in 8a; (c) Image simulation computed for a 0.2 nm thick crystal at -54 nm defocus; (d) Corresponding structural model used to calculate (c).

III.2. Determination of the Stoichiometry of the Progressively Reduced WO_{3-x} Particles by XRD

Irrespective of their morphology, the stoichiometry of the WO_{3-x} precursors, could not be easily assigned by XRD (3b, 5). First, most of the samples were either not sufficiently crystalline or were of too small particle size for generating well-defined XRD patterns. Moreover, several non-stoichiometric tungsten oxide phases have been reported in the literature and all of them exhibit very similar patterns. Consequently, assigning the stoichiometry of the WO_{3-x} phases comprehensively from XRD data alone was a rather difficult task. The measurement by electron diffraction was more informative in this case. Individual crystallites or groups of crystallites were examined within the TEM. The absence of such ED pattern in the case of type I precursor shows that many of the nanoparticles are amorphous (although lattice images indicated that many of these particles were nanocrystalline), as was clearly evidenced by the XRD measurements. By contrast, type II nanoparticles diffract strongly enough, to the extent that bulk XRD patterns could be obtained and therefore the values of the d_{hkl} spacings could be calculated. The stoichiometry of individual particles of type II precursors can be ascribed to the tetragonal phase $W_{20}O_{58}$ ($WO_{2.9}$) as described recently by Sloan *et al.* (5). This $W_{20}O_{58}$ ($WO_{2.9}$) phase corresponds to the usual stacking of WO_3 with randomly distributed defects along the whisker axis consisting predominantly of CS-type or related defects.

The two sets of XRD measurements originating from both types of precursors are summarized in Table 2. The phases are globally consistent with those identified in the ED patterns, except for the most difficult part, which is the assignment of the stoichiometry of the long tungsten oxide whiskers. Indeed, while the samples consisting of long oxide whiskers were ascribed by XRD to the phase $W_{18}O_{49}$, the same sample was found to consist of a mixture of phases $W_{20}O_{58} + W_nO_{3n-1}$ ($n = 4, 5, 6$), by the ED analysis. This point is particularly relevant since $W_{18}O_{49}$ was definitely detected in the same batches by HRTEM. The proportion of this specific phase compared to the others W_nO_{3n-1} or W_nO_{3n-2} cannot be readily estimated by HRTEM, due to the poor statistics of this method. The fact that the XRD patterns of the reaction product exhibit only the $W_{18}O_{49}$ phase and not the W_nO_{3n-1} or W_nO_{3n-2} phases could be related to either a major proportion of the $W_{18}O_{49}$ phase, which is unlikely, or to its larger cross section for X-ray diffraction. Therefore, the evolution of the tungsten suboxide nanowhiskers along the reduction process does not lend itself for an exclusive formation and evolution of $\{hkl\}_R$ CS planes, as was previously assumed (5). (Nevertheless, the $W_{18}O_{49}$ phase, which is organized around pentagonal columns originates also from the presence of $\{001\}_R$ CS planes. This point emphasizes the fact that the tungsten suboxides phases are systematically related to $\{001\}_R$ CS planes, which develop along the whisker growth axis).

TABLE 2
Influence of the Reduction Time on the Stoichiometry of the WO_{3-x} Particles (types I and II Precursors)

Type I precursor (spherical-faceted particles)		Type II precursor (needle-like particles)	
Reduction time (min)	XRD	Reduction time (min)	XRD
2	$W_{18}O_{49}$	1	$W_{18}O_{49}$
5	WO_2	5	$W_{18}O_{49} + W$
10	WO_2	10	$W_{18}O_{49} + W$
15	WO_2	20	$WO_2 + W$
60	$WO_2 + W$	60	W

Figure 9 shows the XRD patterns of the two oxide nanowhisker phases obtained by the fluidized bed reactor. While Fig. 9a shows the XRD pattern of the HC-W_5O_{14} nanowhiskers, Fig. 9b shows the XRD pattern of the $W_{18}O_{49}$ phase encapsulated by the WS_2 closed layers. Note that the contribution of the encapsulating WS_2 layers to the XRD pattern of this sample is not appreciable. In contrast, the HC-W_5O_{14} phase, which was not encapsulated by sulfide layers, exhibited a very pronounced signal of WS_2. Unfortuantely, the present product was not a pure nanowhisker phase and contained also substantial amounts of fullerene-like WS_2 nanoparticles, which contributed a component to the XRD signal.

III.3. Raman Measurements

By recording the Raman spectra at different stages of the nanotube synthesis, it was possible to monitor the reduction and sulfidization processes when converting polycrystalline WO_3 into WS_2 nanotubes, as shown in Fig. 10 (3a). These spectra show that, in principle, one should be able to follow the transformation of the remaining tungsten oxide nanoparticles in the core of the WS_2 nanotubes by this technique. Unfortunately, the strong absorption and the Raman scattering by the WS_2 envelope suppresses the Raman signal from the oxide core at the wavelength used in these experiments (632.8 nm). The Raman spectrum of WS_2 nanotubes was compared to that of bulk 2H-WS_2 material before (20). In the next sections, the Raman spectra of oxide nanowhiskers, which were prepared by similar techniques, is reported.

III.3.a. Evolution of the Raman spectra of type I isotropic faceted WO_{3-x} particles upon reduction. While WO_3 has been extensively studied by this technique (21–24), no report

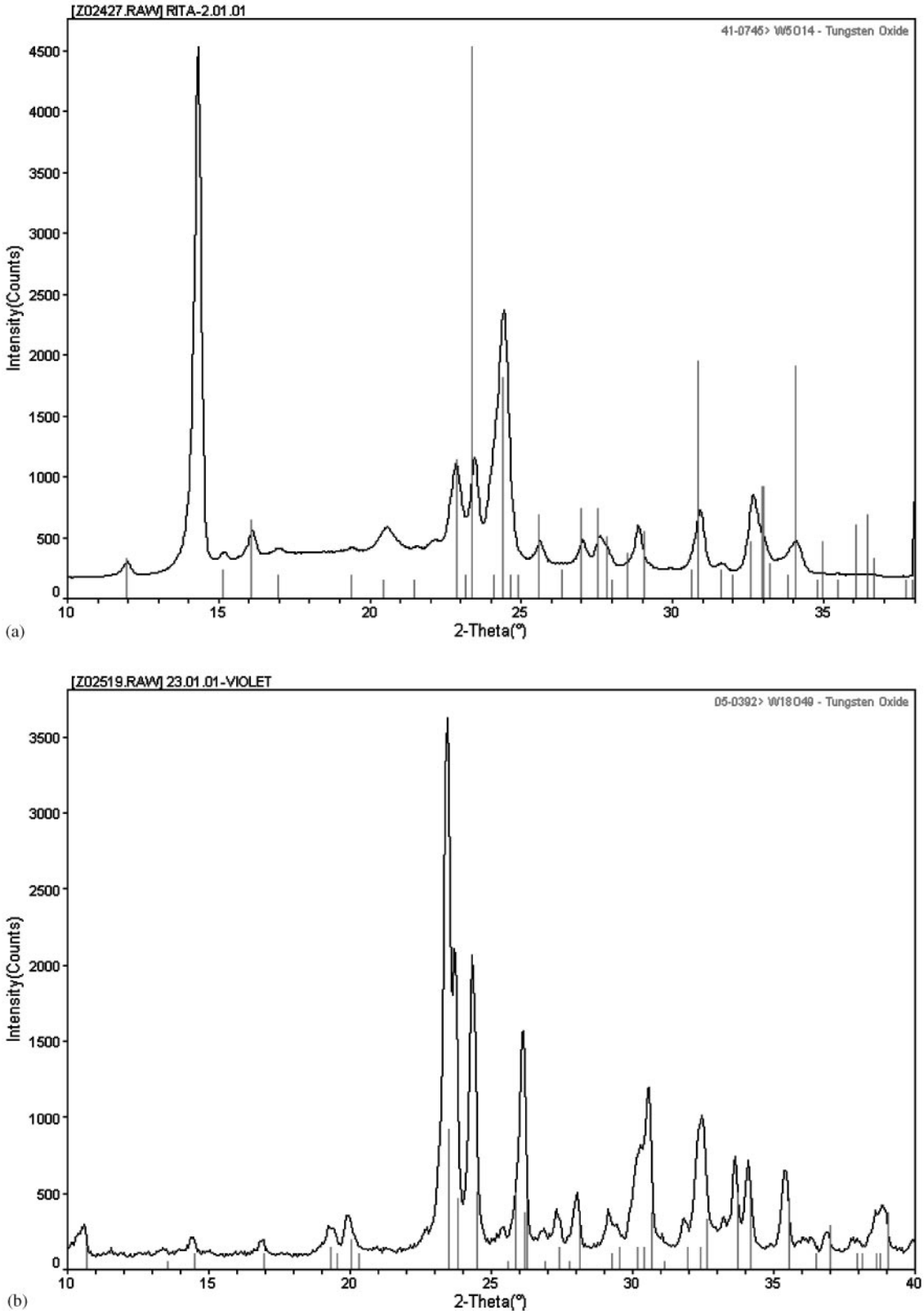

FIG. 9. XRD patterns of two nanowhisker phases obtained by the fludizied bed reactor: (a) HC-W_5O_{14} phase which contained also substantial amounts of fullerene-like WS_2 nanoparticles; (b) Encapsulated $W_{18}O_{49}$ phase encased by a few closed WS_2 layers. The peak at 14.3° belongs to the WS_2 phase.

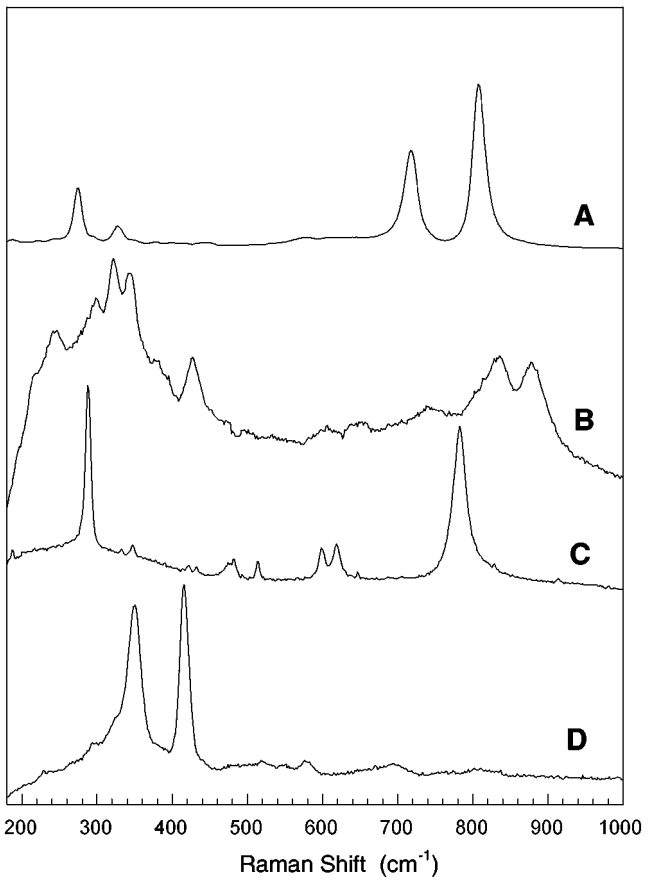

FIG. 10. Raman spectra of (a) WO_3, (b) $WO_{2.9}$ nanoparticles, (c) WO_2, and (d) WS_2 nanotubes.

was apparently published on the Raman of the tungsten suboxide (i.e., WO_{3-x}) phases; a fact, which is probably related to the difficulty of isolating pure phases of tungsten suboxides and therefore in attributing the observed features to the composite structural components. However, with the development of commercial Raman microscopes with a resolution of below 1 μm, the recording of a Raman spectrum of a single nanowhisker has become feasible.

Figure 10 shows the Raman spectra of the isotropic faceted WO_{3-x} nanoparticles reduced at 840°C under the flow of a 1% H_2/99% N_2 for 0, 2, 5, and 60 min. The Raman spectra of type I (spherical nanoparticles) precursor. Figure 11, shows an intense background indicating that the material is amorphous. Upon slight reduction (2 min), a broad feature centered at $\sim 315\ cm^{-1}$ is observed above the background. After 5 min of reduction the Raman spectrum is intense and detailed with Raman lines at: 168(w), 189(w), 286(vs), 345(w), 423(w), 479(m), 512(m), 599(m), 617(m) cm^{-1}, and a mode at 781(s) cm^{-1} which tails to higher energies (w-weak; m-medium; s-strong; vs-very strong). This spectrum has been recently attributed to WO_2

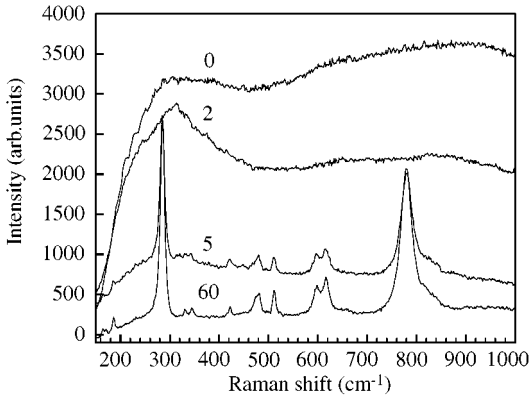

FIG. 11. Raman spectra of type I (spherical) nanoparticles under reduction after different annealing times (in min): the starting precursor is $WO_{2.9}$ and is designated as 0 (min). With longer annealing times (indicated for each curve in min) the Raman spectrum of the nanoparticles resemble more and more that of WO_2 nanoparticles.

(Ref. (3a)). The Raman spectra for the further reduced samples, 10, 20 min (not shown) and 60 min are similar to that obtained after 5 min and correspond to WO_2.

III.3.b. Evolution of the Raman spectra of type II WO_{3-x} nanowhiskers upon reduction. Figure 12 shows the Raman spectra of the needle-like WO_{3-x} particles reduced at 840°C under the flow of a 1% H_2/99% N_2 gas for 1, 5, 10, 20, and 60 min. After 1 min of reduction the needle-like precursor is still amorphous resulting in a featureless Raman spectrum. In the Raman spectrum of the needle-like material reduced for 5 min several new Raman modes are observed in the 200–400 and 800–900 cm^{-1} regions, above an intense

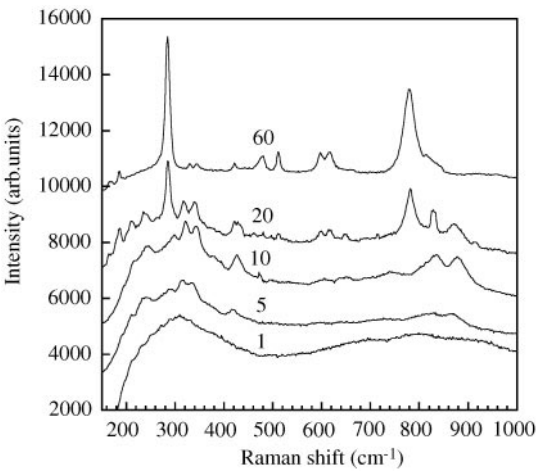

FIG. 12. Raman spectra of type II (whisker) nanoparticles under reduction. The numbers on each curve represent the annealing time in forming-gas atmosphere. After 60 min annealing time the spectrum resembles that of WO_2.

background. In the high-frequency region, two broad bands appear centered at 825 and 870 cm^{-1}. In the lower frequency region of the spectrum, a broad band appears between 200 and 400 cm^{-1} with features at 240, 290, 315, 335, 375, and 418 cm^{-1}. Although the XRD patterns obtained from this needle-like oxide sample indicated that the particles are amorphous (25), the ED patterns and HRTEM images revealed that this phase has a highly distorted layered structure (26). After 10 min of reduction, the Raman spectrum does not change relative to that obtained after 5 min, but the features become more clearly pronounced. Reducing the needle-like precursor for 20 min results in a low background and several new modes in the Raman spectrum appear, as follows: (i) three bands in the high frequency region at 782, 830, and 870 cm^{-1}, (ii) several bands in the low frequency region at 186(w), 210(w), 237 (m), 283(vs), 318(m), 340(m) cm^{-1}, and (iii) several new bands in the central region of the spectrum at: 425(m), 511(w), 600(w), 620(w), and 650(w) cm^{-1}. The Raman spectrum of the fully reduced type II precursor (60 min) is similar to that observed for the fully reduced type I precursor (Fig. 10, 60 min annealed) and is assigned to WO_2. Similar features, i.e., changes in relative peak intensities, shifts in band positions and new modes, were observed when following the reduction process of MoO_3 by *in situ* Raman spectroscopy (27).

Figure 13 shows the Raman spectra of a nanowhisker, which was produced by the fluidized bed reactor and according to XRD belongs to the phase HC-W_5O_{14}. Raman peaks are observed at 215, 264, 325, 349, 418, 425, 707, and 800 cm^{-1}. In other nanowhiskers of this kind a series of peaks at 764, 854, and 900 cm^{-1} were recorded as well. Also, because this phase contained also fullerene-like WS_2 nanoparticles, which were in close proximity to the specific nanowhisker, they also contributed to the Raman scattering and their spectrum was superimposed on the spectrum of the oxide nanowhisker. Unfortunately, the Raman spectrum of the $W_{18}O_{49}$ nanowhisker encapsulated with a few WS_2 layers coincided with that of WS_2 nanotubes (3a). In this case the scattering intensity of the encapsulating WS_2 phase is rather strong and suppressed the Raman spectra from the oxide cores.

III.3.c. Discussion of the Raman spectra of the reduced WO_{3-x} particles (type I and type II particles). Since solid state Raman scattering is sensitive to both metal–oxygen bond length, coordination number, and symmetry around a metal center, it is therefore a useful technique in studying phase transformation and evolution within these types of compounds.

Recently, the Raman spectra of transition metal oxides has been interpreted using the diatomic approximation which regards each metal–oxygen bond in the material as vibrationally independent of its surroundings (25). Consequently, in tungsten oxides constructed from WO_6 octahedral repeat units, all Raman bands around 400 cm^{-1} are assigned to W–O stretching modes and are assumed to directly reflect the W–O bond lengths. An empirical expression for relating the W–O bond length to the frequency of the Raman modes, which enables a direct determination of the W–O bond length from the Raman spectra, is derived (25). Furthermore, the energy of the highest observed Raman band associated with the stretching of the shortest W–O bond reflects the regularity of the structure (25, 26); i.e., for the different octahedrally coordinated WO_x phases,

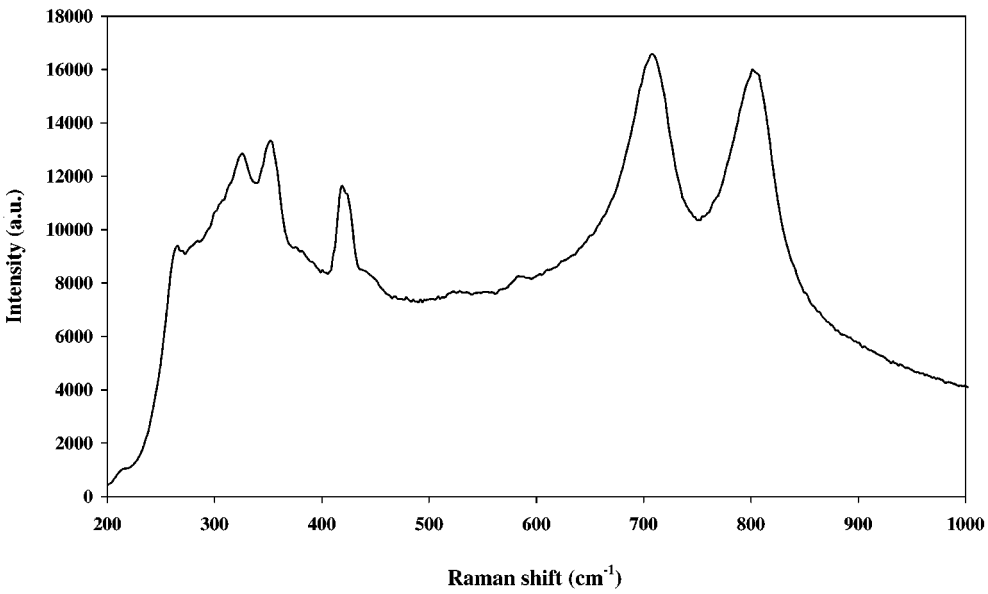

FIG. 13. Raman spectrum of a CS-W_5O_{14} nanowhisker flanked by WS_2 nested fullerene-like nanoparticles.

a higher Raman stretching mode indicates a more distorted structure. By comparing the Raman spectra of several tungsten oxide compounds with an octahedral coordination, Horsley *et al.* (25) showed that the distorted octahedra possess Raman bands between 740 and 980 cm^{-1}.

The room temperature crystallographic structure of WO_3 is derived from the ReO_3 structure with the corner-shared octahedra tilted, and the tungsten atoms distorted from their symmetrically located positions within the oxygen octahedra, to form zig-zag chains with alternating short and long W–O bond distances. The crystalline WO_3 Raman spectrum (Fig. 5a) exhibits major Raman bands at 808, 719, and 275 cm^{-1}, where the 808 and 719 cm^{-1} are assigned as W–O–W stretching frequencies and the 275 cm^{-1} as a W–O–W bending mode (25). The shorter W–O–W bonds are responsible for the stretching mode at 808 cm^{-1}, while longer bonds, are the source of the 719 cm^{-1} peak. Relatively strong peaks are also observed around 300 cm^{-1} and below 150 cm^{-1} attributable to W–O deformation and O–O deformation modes, respectively.

WO_2 has a distorted rutile structure formed by edge sharing WO_6 units and metal-metal bonds (28, 29). The most intense peak in the Raman spectra of WO_2 (Figs. 10, 11d, and Fig. 12e) at 285 cm^{-1} is assigned to the W–O–W bending mode, which appears at 275 cm^{-1} for WO_3 (Fig. 10). The shift of this band to a higher frequency is attributed to the constrained W–O–W bending in the more compact distorted-rutile structure of WO_2 (30). Only one stretching mode is observed for WO_2 at 782 cm^{-1}. This mode exhibits, however, a strong asymmetric tailing to higher energies. Hence, the WO_6 octahedra forming the rutile structure are highly distorted and contain a large variety of W–O–W bond lengths.

Upon reduction of WO_3, oxygen vacancies are formed which are compensated by either crystal shear planes (CS) or pentagonal columns structures (PC). In the CS structure $\{102\}_R$, $\{103\}_R$ crystal-shear planes, along with $\{001\}_R$ CS planes of the W_nO_{3n-1} series were observed [5]. The CS planes are formed by the edge-sharing of neighboring octahedra. Two adjacent CS planes are separated by a comparatively undistorted WO_3 sublattice. In the PC structures (HC-W_5O_{14}, $W_{12}O_{34}$, and $W_{18}O_{49}$), pentagonal columns couple in pairs by edge-sharing octahedra to form "tunnel compounds." Wide, empty pseudo-hexagonal tunnels are formed which run through the structure. While WO_3 has been extensively studied by Raman spectroscopy, the tungsten suboxides, in general, and more particularly, the homologous series with the formula W_nO_{3n-1}, were not studied with Raman spectroscopy, to the best of our knowledge, probably because it is difficult to isolate any pure phase of the suboxides (5).

From the evolution of the Raman spectrum of precursor I, upon reduction, it is evident that the isotropic faceted WO_{3-x} particles are rapidly reduced to WO_2. The fact that the intermediate nonstoichiometric phases do not produce distinct Raman spectra indicate that the reduction process does not advance through a set of well defined phase transformations.

The reduction of the needle-like precursor, on the other hand, is slower and proceeds through nonstoichiometric phases with detailed Raman spectra (Fig. 12). The Raman spectrum of the reduced precursor contains features similar to that of WO_3, namely, two broad bands in the 800–900 cm^{-1} region and several bands in the 200–400 cm^{-1} region. The 825 and 870 cm^{-1} modes are assigned to the W–O–W stretching modes which are shifted to higher energies compared to WO_3. This shift is the outcome of the shorter W–O–W bonds introduced by the edge-sharing octahedra. Using the empirical formula described in (24), it is possible to associate the 870 cm^{-1} mode with the stretching mode of a 1.78 Å W–O bond. This value compares favorably with the calculated distance of 1.77 Å for one of the W–O bond lengths in the CS W_3O_8 structure (31). The abundance of many bands in the W–O–W bending region (200–400 cm^{-1}), compared to only one in the WO_3 parent material, indicates that there are several distinct W–O–W bond lengths. The complex structure of the PC phases, mainly, $W_{18}O_{49}$, contain a wide range of W–O–W bond lengths which are expected to result in a very broad, featureless band. The CS structures, however, contain several possible members of the W_nO_{3n-1} homologous series with different CS distance which could result in specific bending modes. Hence, the Raman spectra of the partly reduced needle-like particles could be a finger-print of the CS structures, although, the contribution of the PC phases, mainly in $W_{18}O_{49}$ and HC-W_5O_{14}, could not be ruled out.

Upon further reduction of the type II precursor, WO_2 is formed. Hence, the Raman spectrum of the type II precursor reduced for 20 min coincides with the Raman spectrum of the CS structure and that of WO_2 (Fig. 12).

The results described previously reflect the fact that along the reduction process, type I and type II precursors undergo a distinguishable evolution since the Raman spectra differ after a few minutes reduction. In the case of type II precursors, for which the reduction process leads in a first step to the formation of multiple W_nO_{3n-1} phases in a single batch, it has been suggested that each of these phases contribute to new set of Raman peaks, which are related to W–O bond lengths different from those in the $WO_{2.9}$ precursor. However, it is not easy to attribute each of these peaks to a certain W–O bond length. Computer simulation of each of the W_nO_{3n-1} phases might be very useful in this case.

The Raman spectrum of the HC-W_5O_{14} phase shows three peaks in the W–O–W stretch region at 707, 800, and 900 cm^{-1}. The position of the first two peaks (707 and 800 cm^{-1}) is similar to the position of the W–O–W stretch peaks observed for the WO_3 starting material. However, the peaks are broader and the relative intensity changes. While

the 800 cm^{-1} peak dominates the WO_3 Raman spectrum, in the Raman spectrum of HC-W_5O_{14}, the 800 cm^{-1} peak is very broad and has lower intensity than the 707 cm^{-1} peak. The decrease of the 800 cm^{-1} peak could be correlated with the appearance of the new peak at 900 cm^{-1}. Using the empirical formula in (17), the 900 cm^{-1} mode is associated with a 1.76 Å W–O bond. As mentioned earlier, a higher Raman stretching mode wavenumber indicates a more distorted structure. Hence, the reduction of the oxide whiskers effected mainly the shorter W–O bonds. The elimination of oxygen causes the remaining short W–O bonds to shrink even further, while the longer W–O bonds are only slightly altered. This structural change detected by the Raman spectrum is associated with the formation and propagation of the CS planes. The longer W–O bonds reflect the WO_3 sublattice situated in between adjacent CS planes, while the shorter W–O bonds are the result of CS planes forming upon reduction. In the further reduced phase, CS-W_3O_8, the distance between two adjacent CS is small and causes the distortion of all W–O bonds. The distorted structure results in broadening and shifting of the two main W–O stretch modes to 825 and 870 cm^{-1} as shown in Fig. 11.

The absence of Raman bands around 950 cm^{-1} for all measured samples, indicates that, as expected, the heated WO_{3-x} powders do not contain any hydrated phases. The proposed growth mechanism of the needle-like oxides suggests that presence of water molecules, which are formed during the reduction process, enhances the growth of the nanowhiskers (32). Volatile hydrated clusters ($WO_{3-x} \cdot nH_2O$) are formed and subsequently condense on the nanowhisker tip. It is evident from the Raman spectra, however, that the hydrated clusters are reduced upon condensation on the tip and the suboxide nanowhiskers are not hydrated.

IV. CONCLUSIONS

Studies of three types of WO_{3-x} nanoparticles (type I—spherical-faceted and type II—needle-like and commercially available WO_3 nanoparticles), by a combined approach (HR)TEM, XRD, and Raman spectroscopy, has allowed both the morphological evolution of the particles as well as their stoichiometry during the reduction by hydrogen to be followed.

First, it was demonstrated that, irrespective of the starting precursor, WO_{3-x} nanowhiskers are produced during the reduction process. In particular, type I nanoparticles do not sustain their morphology under hydrogen flow.

Second, the needle-like tungsten suboxide phases (type II), and the oxide nanowhiskers produced by the fluidized bed reactor were also found to include the γ-$W_{18}O_{49}$ and W_5O_{14} phases, which contain an ordered array of PC and HC features. On the other hand, the phases W_nO_{3n-1} and W_nO_{3n-2}, consist of ordered $\{001\}_R$ CS planes, only. Since PC + HC phases emanate from suboxide phases containing $\{001\}_R$ CS planes, these kind of CS planes are likely to be present in the beginning of the reduction process of the oxide nanowhiskers, irrespective of their future evolution. However, nothing can be put forward concerning the type I particles, since they change their morphology into nanowhiskers and subsequently into crystalline nanoparticles in the early stages of the reduction process.

Moreover, it has been shown up that different tungsten suboxide phases belonging to the homologous series W_nO_{3n-1} (with $n = 3, 4, 5, 6$) are formed as intermediate stages in the first step of the reaction (ED). This has been confirmed in one specific example by Raman spectroscopy, for which a W–O = 1.77 Å distance, characteristic of a W_3O_8 structure has been calculated by the method of Hardcastle and Wachs (25).

The oxide nanowhiskers which form in the fluidized bed reactor tend to be long and crystalline, which explain the open tip of the WS_2 nanotubes obtained after sulfidization of the nanowhiskers. Most of the encapsulated nanowhiskers obtained in this reaction contain the γ-$W_{18}O_{49}$ phase with a network of PC and HC features.

ACKNOWLEDGMENTS

We are grateful to Alisa Band and Alex Margolin for their technical help with the Raman and XRD measurements, respectively. This work was supported by the ACS-PRF (USA); Krupp Foundation, and France-Israel R & D Foudation (AFIRST). J.S. is indebted to the Royal Society.

REFERENCES

1. (a) Y. Feldman, G. L. Frey, M. Homyonfer, V. Lyakhovitskaya, L. Margulis, H. Cohen, G. Hodes, J.L. Hutchison, and R. Tenne, *J. Am. Chem. Soc.* **118,** 5362 (1996); (b) Y. Feldman, V. Lyakhovitskaya, and R. Tenne, *J. Am. Chem. Soc.* **120,** 4176 (1998).
2. (a) Y. Feldman, E. Wasserman, D. J. Srolovitz, and R. Tenne, *Science* **267,** 222 (1995); (b) A. Zak, Y. Feldman, V. Alperovich, R. Rosentsveig, and R. Tenne, *J. Am. Chem. Soc.* **122,** 11,108 (2000).
3. (a) A. Rothschild, G. L. Frey, M. Homyonfer, M. Rappaport, and R. Tenne, *Mat Res. Innovat.* **3,** 145 (1999); (b) A. Rothschild, J. Sloan, and R. Tenne, *J. Am. Chem. Soc.* **122,** 5169 (2000).
4. Y. Q. Zhu, W. K. Hsu, N. Grobert, B. H. Chang, M. Terrones, H. Terrones, H. W. Kroto, and D. R. M. Walton, *Chem. Mater.* **12,** 1190 (2000).
5. J. Sloan, J. L. Hutchison, R. Tenne, Y. Feldman, T. Tsirlina, and M. Homyonfer, *J. Solid State Chem.* **144,** 100 (1999).
6. T. Miyano, M. Iwanishi, C. Kaito, and M. Shiojiri, *Jpn. J. Appl. Phys.* **22,** 863 (1983) and references therein.
7. E. Iguchi, *J. Solid State Chem.* **23,** 231 (1978).
8. A. Magneli, *Ark. Kemi.* **1,** 223 (1950).
9. M. Lundberg, *Chem. Common. Univ. Stockholm* **12** (1971).
10. W. Sahle, *J. Solid State Chem.* **45,** 324 (1982).
11. I. J. McColm, R. Steadman, and S. J. Wilson, *J. Solid State Chem.* **23,** 33 (1978).

12. Y. Feldman, A. Zak, R. Popovitz-Biro, and R. Tenne, *Solid State Sci.* **2,** 663 (2000).
13. R. Rosentsveig, A. Margolin, Y. Feldman, R. Popovitz-Biro, and R. Tenne, submitted.
14. R. C. Weast (Ed.), "Handbook of Chemistry and Physics," 69th ed., P. B-141. CRC Press, Boca Raton, FL, 1988.
15. P. Gadó, *Acta Phys. Hung.* **18,** 111 (1965).
16. S. Iijima, *J. Solid State Chem.* **14,** 52 (1975).
17. A. Magneli, *Acta Chem. Scand.* **1,** 501 (1948).
18. L. A. Bursill and B. G. Hyde, *J. Solid State Chem.* **4,** 430 (1972).
19. (a) J. D. Donnay and D. Harker, *Amer. Miner.* **22,** 446 (1937); (b) A. S. Myerson, *in* "Molecular Modeling Applications in Crystallization" (A. S. Myerson, Ed.). Cambridge Univ. Press, Cambridge, 1999.
20. G. L. Frey, R. Tenne, M. J. Matthews, M. S. Dresselhaus, and G. Dresselhaus, *J. Mater. Res.* **13,** 2412 (1998).
21. E. Salje, *Acta Crystallogr. Sect. A* **31,** 360 (1975).
22. M. Arai, S. Hayashi, K. Yamamoto, and S. S. Kim, *Solid State Comm.* **75,** 613 (1990).
23. S. Hayashi, H. Sugano, H. Arai, and K. Yamamoto, *J. Phys. Soc. Jpn.* **61,** 916 (1992).
24. M. Scheithauer, R. K. Grasseli, and H. Knözinger, *Langmuir* **14,** 3021 (1998).
25. F. D. Hardcastle and I. E. Wachs, *J. Raman Spectrosc.* **26,** 397 (1995).
26. J. A. Horsley, I. E. Wachs, J. M. Brown, G. H. Via, and F. D. Hardcastle, *J. Phys. Chem.* **91,** 4014 (1987).
27. G. Mestl, P. Ruiz, B. Delmon, and H. Knözinger, *J. Phys. Chem.* **98,** 11,269 (1994).
28. A. F. Wells, *in* "Structural Inorganic Chemistry," 5th ed., p. 541. Oxford Scientific Publications, Clarendon Press, Oxford, 1984.
29. F. A. Cotton and G. Wilkinson, *in* "Advanced Inorganic Chemistry," 5th ed. p. 808. Wiley Interscience, New York.
30. F. H. Jones, R. G. Egdell, A. Brown, and F. R. Wondre, *Surf. Sci.* **374,** 80 (1997).
31. The W–O bond lenghts were calculated using the program "CrystalMaker" (1994–2001 David Palmer).
32. (a) T. Millner and J. Neugebauer, *Nature* **163,** 602 (1949); (b) V. K. Sarin, *J. Mater. Sci.* **10,** 593 (1975).